Journal of
Applied Crystallography
ISSN 0021-8898

Received 16 August 2006
Accepted 21 December 2006

Structure of nickel nanoparticles in a microcrystalline cellulose matrix studied using anomalous small-angle X-ray scattering

Kari Pirkkalainen,[a] Ulla Vainio,[a]* Kaisa Kisko,[a] Tiiu Elbra,[b] Tomas Kohout,[b] Nina E. Kotelnikova[c] and Ritva Serimaa[a]

[a]Division of X-ray Physics, Department of Physical Sciences, University of Helsinki, Finland, [b]Division of Geophysics, Department of Physical Sciences, University of Helsinki, Finland, and [c]Institute of Macromolecular Compounds, Russian Academy of Sciences, St Petersburg, Russian Federation. Correspondence e-mail: ulla.vainio@helsinki.fi

Nickel nanoparticles were synthesized by adding aqueous nickel salt into a microcrystalline cellulose matrix. The Ni^{II} ions were reduced with either sodium borohydride, $NaBH_4$, or potassium hypophosphite, KH_2PO_2, in water or aqueous NH_3 medium. The mass fraction of Ni in the samples was between 3.7 and 8.9%. X-ray absorption spectra at the Ni *K*-edge showed that Ni was partially oxidized only in a sample reduced with $NaBH_4$. Wide-angle X-ray scattering results showed that nickel was in nanocrystalline or amorphous form in the samples. Upon heating fcc Ni, hcp Ni, NiO, Ni_3P and other Ni–P phases formed depending on the reduction parameters. Using anomalous small-angle X-ray scattering the nanometre-scale particle size distributions of the Ni particles were determined. A large fraction of particles less than 15 nm in size were observed in the samples reduced in aqueous ammonium compared with the samples reduced in water. Particles reduced in aqueous ammonium had a large ferromagnetic component.

1. Introduction

The magnetic properties of nanoparticle materials are fundamentally different from the magnetic properties of bulk materials. For example, materials that are ferromagnetic in bulk can behave superparamagnetically as nanoparticles, when the size of the nanoparticle is less than the single domain size (Leslie-Pelecky & Rieke, 1996). For single domain nanoparticles a correlation between the magnetic properties and the size has been observed (Gong *et al.*, 1991). Furthermore, also the crystal structure, the crystallinity, the size distribution, the shape of the nanoparticles and the proximity of the neighboring particles affect the response of the material when a magnetic field is applied to it (Leslie-Pelecky & Rieke, 1996). By dispersing nanoparticles into a matrix the distance between neighboring particles can be manipulated.

Recently, nickel nanoparticles have been the topic of a number of studies owing to their applications as catalysts and magnetic materials. Metallic nickel as well as nickel oxide, boride and phosphide nanoparticles have been prepared (Illy *et al.*, 1999; Xie *et al.*, 2005). In many studies the nanoparticles have been self-supported (Leslie-Pelecky & Rieke, 1996), but also nanocomposite materials where the nanoparticles are in *e.g.* a polymer matrix have been made (Sarkar *et al.*, 2005).

Chemical reduction of Ni^{II} ions by sodium borohydride, $NaBH_4$, in aqueous solution has proved to be a fast and an economical method of nickel nanoparticle production (Goia & Matijević, 1998). The effects of the reaction conditions on the nanoparticles in the borohydride reduction process were studied systematically by Glavee *et al.* (1994). According to their study, weakly ordered metallic nickel and nickel oxide were produced in ambient conditions in aqueous medium while amorphous Ni_2B was obtained in inert atmosphere. Upon heating nickel crystallized to the stable face-centered cubic (fcc) Ni phase. On the other hand, hexagonal-close packed (hcp) nickel nanoparticles have been prepared using the borohydride reduction in organic solvents (Illy *et al.*, 1999). It was found that particles of size 1–4 nm had hcp structure, while larger particles had fcc structure. Later Roy *et al.* (2005) also prepared nickel nanoparticles by borohydride reduction in water in ambient conditions, but instead of hcp nickel nanoparticles they obtained yet another crystalline structure, which they identified as tetragonal with an O atom sitting in the middle of the unit cell.

Reduction with sodium hypophosphite, NaH_2PO_2, has been used previously for making of nickel and nickel phosphide particles in inert conditions (Xie *et al.*, 2005). It was observed that the particle size could be controlled through the ratio $H_2PO_2^-/Ni^{2+}$ so that small particles had a large phosphorus content and *vice versa*. The smallest particles were amorphous and 27 nm in diameter on the basis of transmission electron microscopy. Upon heating, crystalline phases of fcc Ni and tetragonal Ni_3P developed.

Electron microscopy has been used extensively to study the morphology of magnetic transition metal nanoparticles. In the case of crystalline particles the crystal structure and the average size of crystallites has been obtained with X-ray diffraction. Anomalous small-angle X-ray scattering (ASAXS) gives valuable bulk information on the average inter-particle distance or the particle size distribution (Simon & Lyon, 1994; Bazin *et al.*, 1997). Recently ASAXS has been used to determine the particle size distribution of amorphous nickel phosphide nanoparticles (Tatchev *et al.*, 2005). X-ray absorp-

Table 1
Mass fraction of Ni in the samples (% Ni) determined by X-ray absorption spectroscopy.

The error given is the maximum error. Ratio is the molar ratio BH_4^-/Ni^{2+} or correspondingly $H_2PO_2^-/Ni^{2+}$, while Ni^{2+}/MCC is the molar ratio of Ni^{2+} ions to the MCC monomer unit.

Number	Medium	Ni^{2+}/MCC	Reducer	Ratio	% Ni
1	H_2O	0.33	$NaBH_4$	3	8.9(6)
2	H_2O	0.33	KH_2PO_2	23	5.0(4)
3	$NH_3{\cdot}H_2O$	0.33	KH_2PO_2	23	3.7(3)
4	$NH_3{\cdot}H_2O$	0.45	KH_2PO_2	34	6.5(5)

tion gives information on the oxidation state and the chemical bonding of transition metal atoms in nanoparticles (Modrow, 2004). Ideally, the magnetic properties of the samples can be correlated with the structure of the nanoparticles.

In this work we demonstrate the possibility to use cellulose as a support for nickel nanoparticles. Anomalous small-angle X-ray scattering, wide-angle X-ray scattering (WAXS), X-ray absorption spectroscopy and scanning electron microscopy (SEM) were used to study the structure and morphology of nickel nanoparticles embedded in a cellulose matrix. The magnetic properties of the samples were studied using a vibrating sample magnetometer (VSM).

2. Methods

2.1. Samples

Nickel or nickel phosphide nanoparticles were synthesized into a microcrystalline cellulose (MCC) matrix by diffusion of nickel ions, Ni^{2+}, from a solution of $NiSO_4{\cdot}7H_2O$ and subsequent reduction of Ni^{2+}. The microcrystalline cellulose was prepared by mild acid hydrolysis. The cellulose was bone-dried and contained moisture less than 1 mass%. Sodium borohydride, $NaBH_4$ ('Ferak', Berlin), and potassium hypophosphite, $KH_2PO_2{\cdot}H_2O$ ('Vecton', Russia), were used as reducers. All chemicals were analytical grade. Diffusion of Ni^{2+} to the MCC matrix was carried out under intensive stirring of 1 g of MCC in 20 ml of H_2O or aqueous ammonium solution of $NiSO_4{\cdot}7H_2O$ for a period of 1 h. The concentration of the $NiSO_4{\cdot}7H_2O$ solution varied from 0.05 to 0.135 *M*. The concentration of ammonium, which played the role of a ligand in the nickel–ammine complex $[Ni(NH_3)_n]^{2+}$, was not higher than $n = 5$–6. A 20 ml aqueous solution of one of the reducers was added to the suspension. The reduction was carried out under intensive stirring at 293 K for 1 h (with $NaBH_4$) or at 368 K for 3 h (with $KH_2PO_2{\cdot}H_2O$). After reduction the powder samples were isolated from the suspensions, thoroughly rinsed with water and ethanol, and dried in vacuum at 313 K. They were gray or black and were stable in ambient conditions. The samples selected for this study are listed in Table 1.

2.2. Scanning electron microscopy

In the micrometre range the morphology of the samples was studied by scanning electron microscopy using a Jeol JCM-35 CF (Jeol, UK) instrument. To obtain micrographs, the samples were mounted on an aluminium support covered with a carbon layer in a special chamber and sputtered under inert gas using a gold target.

2.3. Wide-angle X-ray scattering

WAXS measurements were carried out in the perpendicular transmission geometry using Cu $K\alpha_1$ radiation. A setup with a Rigaku rotating-anode (fine focus) X-ray tube and a MAR345 image-plate detector was used. The beam was monochromated and focused to the detector with a bent Si(111) crystal and a totally reflecting mirror. The samples were heated *in situ* under helium atmosphere with a Linkam heating stage. Samples 1 and 4 were heated at 10 K min^{-1}, measured for 30 min at constant temperatures 323, 373, 423, 473, 523, 573, 623 and 673 K, and thereafter cooled back to room temperature more rapidly. Before each measurement the temperature was stabilized for 10 min. Samples 2 and 3 were measured similarly at temperatures 323, 523, 573, 623 and 673 K.

The intensities were corrected for absorption and a geometrical correction to compensate for the detector flatness was applied. The angular range was calibrated with silver behenate and silicon. The instrumental broadening was determined to be 0.22° at 47° and 0.19° at 28.4°.

The average size of the crystallites, B_{hkl}, was determined using the Scherrer formula (Guinier, 1994). The intensity maxima were fitted with Gaussian functions.

2.4. X-ray absorption

Anomalous small-angle X-ray scattering and X-ray absorption measurements were conducted at the experimental station JUSIFA B1 at Hamburg Synchrotron Radiation Laboratory (HASYLAB) in Germany (Haubold *et al.*, 1989). The samples were measured *in vacuo*.

The X-ray absorption near-edge structure (XANES) at the Ni *K*-edge was determined by measuring the flux of the direct beam and of the beam transmitted by the sample with a diode. The energy scale was calibrated by using the first inflection points in the spectra of Co, Ni, Cu and Ag foils (Kraft *et al.*, 1996). The anomalous scattering factors f' and f'' were determined for the samples 1 and 3 by measuring X-ray absorption at an energy interval of 7900–9200 eV.

The mass fraction of Ni in the samples (Table 1) was calculated from the Ni *K*-absorption edge by comparing the experimental and theoretical (291 g cm^{-2}; Chantler *et al.*, 2005) edge jumps.

2.5. Anomalous small-angle X-ray scattering

The ASAXS data were collected using a multi-wire area detector at four photon energies below the *K*-absorption edge of Ni. Sample-to-detector distances of 935 and 3635 mm were used. A sample of glassy carbon was measured at each energy for absolute intensity scale (cm^{-1}) calibration. The measurement time per sample per energy was from 5 to 15 min. The magnitude of the scattering vector is defined as $q = 4\pi \sin\theta/\lambda$, where λ is the wavelength and 2θ is the scattering angle. The reliable q range was 0.0125–0.325 $Å^{-1}$.

The software available at the beamline was used to integrate, to correct for absorption and detector sensitivity, to subtract the dark current and the background, and to combine the scattering curves obtained from different distances. It was also used in the absolute intensity scale calibration. An energy-dependent constant was subtracted from each intensity by using *Matlab* so that at large q all intensities followed the Porod law $I \propto q^{-4}$.

2.6. Magnetic properties

Magnetic properties of the pristine samples were measured using a vibrating sample magnetometer 3900 VSM (Princeton Micromag) at room temperature. About 10–30 mg of sample were used in one measurement and the rest of the sample capsule was filled with cellulosic material. The cellulose material was measured separately and its magnetization curve was subtracted from the data. The magnetization values given in this study are normalized to the mass of nickel in the sample, determined with the X-ray absorption method.

The field strengths are given in Tesla and are thus multiplied by the permeability of free space.

3. ASAXS data analysis

The nanocomposites were described as two-component systems consisting of MCC (a) and nickel (b). The X-ray scattering intensity $I(q)$ was then written as (Fuoss *et al.*, 1981; Simon & Lyon, 1994)

$$I(q, E) = x_a|f_a(q, E)|^2 S_{aa}(q) + 2x_b\Re[f_a(q, E)f_b(q, E)]S_{ab}(q) + x_b|f_b(q, E)|^2 S_{bb}(q), \quad (1)$$

where $f(q, E) = f_0(q) + f'(E) + if''(E)$ is the scattering factor, $x_a$and x_b are the atomic fractions of the components a and b, and $S_{aa}(q)$, $S_{ab}(q)$ and $S_{bb}(q)$ are the partial structure factors (PSFs). In the small-angle scattering region we have assumed $f_0 = Z$. For MCC the anomalous scattering factors, f'_a and f''_a, were assumed to be zero.

Differential structure factors (DSFs) were obtained by subtracting two intensities $I(q, E)$ from each other. A DSF is a weighted sum of $S_{bb}(q)$ and $S_{ab}(q)$.

Equation (1) can be presented as a linear equation for each q value as

$$\mathbf{I} = A\,\mathbf{S}, \quad (2)$$

where $\mathbf{I}$ is a column vector of intensities $I(q, E)$, $\mathbf{S}$ is a column vector of the PSFs, and A is the coefficient matrix. It is well known that the problem of solving PFSs from intensity curves measured only at one absorption edge is ill-posed and a good estimate can be obtained only for the Ni–Ni PSF (Simon & Lyon, 1994). Instead of using an analytical formula of this PSF we solved the whole equation to reveal the possible mirror effects in the PSFs (Munro, 1982).

Extraction of the PSFs was attempted by directly solving equation (2), by using the simple Tikhonov regularization technique (Neumaier, 1998; Serimaa *et al.*, 1996) to solve the equation, and by the derivative technique (Fuoss *et al.*, 1981), in which the $S_{bb}(q)$ and $S_{ab}(q)$ PSFs can be obtained by a linear fit to $dI(q, E)/df_b(E)$. These methods were first tested with simulated scattering data, in which statistical errors comparable to the estimated experimental statistical errors had been introduced. The solutions were compared with exact simulated PSFs. The solutions of equation (2) and the derivative method gave clearly erroneous results, indicating that these methods are not applicable to our case because of the level of statistical error in the data. The solution with the Tikhonov regularization, however, gave promising results, and managed to reproduce the exact simulated PSFs with good accuracy. Regularization stabilizes the otherwise ill-posed equation, but it can distort the solutions if used incorrectly. The unity matrix was used as a regularization matrix and the efficiency of regularization was varied by introducing a rising dependence of the regularization parameter with the scattering vector q. This prevented too strong regularization at small q and ensured smoothness of the solution at high q where the statistical errors were larger.

It was established, by trials with the simulated scattering data, that minute errors in the intensities or in the anomalous scattering factors caused mirror effects in the solved PSFs. A method was devised to correct the absolute intensity levels and to obtain an approximate Ni–Ni PSF. The anomalous scattering factors were assumed to be correct and the absolute intensity levels were assumed to be erroneous. Correct absolute intensity levels were searched by an iteration routine that solved the PSFs while continuously scaling the measured intensities with random coefficients around a tolerance of 1%. Only the solutions in which all three PSFs were positive in the region $q = 0.0125$–0.0165Å^{-1} were accepted as physically sound. This assumption was justified by the simulated scattering data, which indicated that all the PSFs should be positive at very small scattering angles. Furthermore, the group of accepted solutions was screened for strong correlations between the three PSFs, and the respective solutions were discarded. Finally, the remaining accepted solutions were averaged and a standard deviation of the summed solutions was calculated. The method produced the Ni–Ni PSF with satisfactory accuracy, the standard deviation was small, and the shape of $S_{bb}(q)$ did not change significantly between different accepted solutions.

Particle size distributions in the nanometre range were solved from Ni–Ni partial structure factors $S_{bb}(q)$ assuming that all particles were spherical and that there were no inter-particle interference effects. For spheres of different sizes the intensity can be written as

$$I(q) = \sum_{n=1}^{N} \nu(R_n) I(q, R_n). \quad (3)$$

Here $\nu(R_n)$ is the volume fraction of spheres of radius R_n, *i.e.* the number distribution, in the sample, while the intensity of a sphere of radius R_n is (Guinier, 1994)

$$I(q, R_n) = \left(\Delta\rho_e \frac{4}{3}\pi R_n^3\right)^2 \frac{9(\sin qR_n - qR_n \cos qR_n)^2}{(qR_n)^6}, \quad (4)$$

where $\Delta\rho_e$ is the electron density difference between the sphere and the surroundings.

The particle size distribution was retrieved from $S_{bb}(q)$ using a Monte Carlo fitting procedure similar to that described by Martelli & di Nunzio (2002) with the modification that spheres of different radius were picked randomly from an array $R_n = \pi/q_n$. In order to reduce statistical error the PSFs were smoothed before fitting.

4. Results and discussion

The pristine samples 1, 2 and 4 were studied with SEM. Spherical particles of various sizes on the surface of fibrous cellulose were observed. Some of the particles were clustered into aggregates (Fig. 1) and were merged together continuously. In sample 1 the particles were less than about 0.14 µm in size, in sample 2 most were less than 0.4 µm but also particles of more than 1 µm in size were observed, and in sample 4 the maximum frequency of the particle size distribution was at 0.25 µm.

The X-ray absorption measurements (Fig. 2) showed that the Ni *K*-edge was at the same position for samples 1–4 as for the Ni foil. A linear background was first fitted to the pre-edge region and subtracted before the XANES spectra were normalized to one at energy 8360 eV. The XANES spectrum of sample 1 resembled that of the Ni foil but showed a maximum typical for oxides indicating that

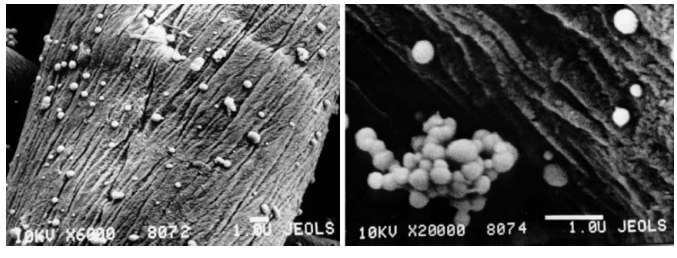

Figure 1
SEM results for sample 4 showing the micrometre-scale structure. The white spheres contain nickel and the matrix is fibrous microcrystalline cellulose. The scale bars are 1 µm in length.

nickel was in metallic and oxidized forms (Mansour & Melendres, 1998). Spectra of samples 2–4 showed smoother features, which indicated that Ni was in weakly ordered nanoparticles.

The nanoparticles were weakly ordered in the pristine samples also on the basis of the diffraction patterns. The diffraction patterns of the pristine samples (Fig. 3) showed only reflections from cellulose and a broad and weak diffraction maximum at $q = 3.09\text{Å}^{-1}$. The maximum could be either the reflection 111 of face-centered cubic Ni or the reflection 011 of hexagonal close-packed Ni (JCPDS files 4–850 and 45–1027), or it could arise from amorphous Ni. The positions of these reflections are the same and it is not possible to conclude which crystalline phase dominates in the nanoparticles. In the study of Glavee *et al.* (1994) both a broad maximum at the same q value of about 3.09Å^{-1} and other broad reflections corresponding to hcp structure can be seen in the diffraction data.

The crystalline arrangement of the MCC matrix had not changed in the chemical processing. The size of cellulose I crystallites in the direction normal to the plane (200) was determined to be 7.2 (1) nm.

Upon heating the samples in helium atmosphere the cellulose crystallites first expanded and finally decomposed (Fig. 3*a*) while crystalline phases of Ni compounds emerged. The expansion of cellulose was not affected by the crystallization of the nanoparticles. For sample 1 the fcc Ni phase crystallized below 573 K after which also maxima possibly arising from the hcp Ni phase were seen at 623 K. After annealing at 673 K and cooling to 303 K only fcc Ni and NiO (JCPDS 78–643) phases remained with NiO in smaller amount. For samples 2, 3 and 4 crystalline NiO was not observed at any stage of the heating (Fig. 3*b*). For samples 2 and 4 a metastable phase (Xie *et al.*, 2005; Hur *et al.*, 1990) and an Ni_3P phase (JCPDS 74–1384) were observed. For details, see Table 2. The temperature behavior of the Ni–P nanoparticles was similar to self-supported Ni–P nanoparticles (Hur *et al.*, 1990). Unlike reported by Hur *et al.* (1990) and Xie *et al.* (2005) we were not able to identify the metastable phase as Ni_5P_2 or $Ni_{12}P_5$ (JCPDS 17–225 and 22–1190).

In order to solve the Ni–Ni partial structure factor from ASAXS data the anomalous scattering factors, f' and f'', were determined from the extended X-ray absorption fine structure spectra of samples 1 and 3 using the program *CHOOCH* 4.0 (Evans & Pettifer, 2001). Table 3 collects both experimental and theoretical (Brennan & Cowan, 1992) values of f' and f'' at the ASAXS measurement energies. According to the simulations with the model nanocomposites a good approximation only for the Ni–Ni PSF could be obtained. The solved Ni–Ni PSFs are presented in Fig. 4 together with the fitted particle size distributions obtained using the Monte Carlo method. The particle size distributions were similar to distributions obtained from DSFs except for the smaller portion of large particles. The particle size distributions show that on the nanometre scale samples 3 and 4 contain smaller particles than samples 1 and 2. The pores of the

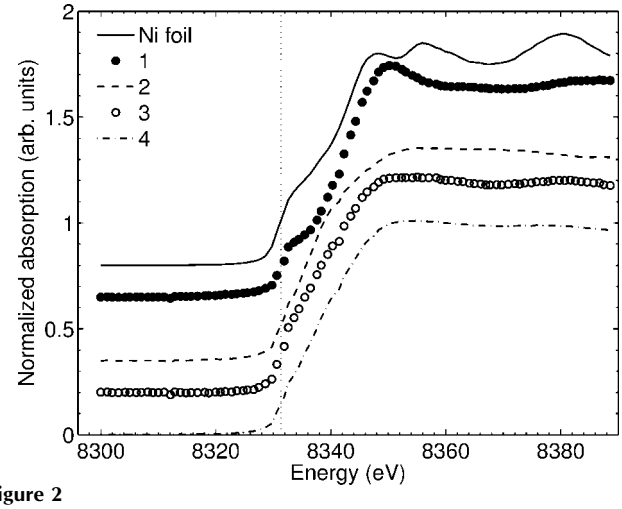

Figure 2
The normalized XANES spectra of the samples and an Ni foil. The curves are shifted vertically for clarity. The vertical line is drawn at the first inflection point of the spectrum of Ni foil.

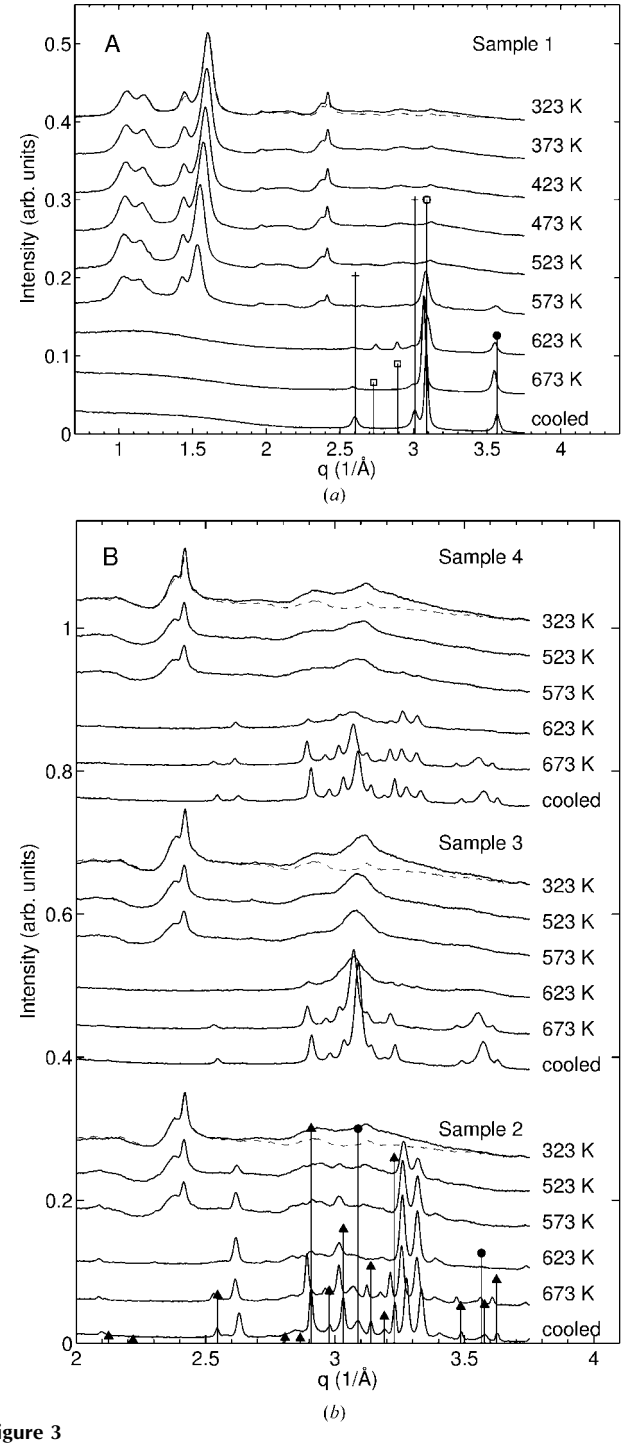

Figure 3
X-ray diffraction patterns of the samples (solid lines) at different temperatures and MCC (dashed lines) at 323 K are shifted for clarity. The theoretical positions and relative intensities of the strongest reflections from NiO (crosses), fcc Ni (filled circles), hcp Ni (open squares) and Ni_3P (filled triangles) are shown. The cellulose reflections disappear upon heating from 573 to 623 K.

Table 2
The crystalline phases recognized from the diffraction patterns upon heating and magnetic parameters of the pristine Ni nanoparticles at 298 K.

The temperature where the crystalline phase was first observed is given. Symbol *m* refers to the metastable phase(s). For samples 1 and 2 the magnetic parameters are from data from which paramagnetism was removed.

Number	fcc Ni	hcp Ni	NiO	*m*	Ni_3P	H_c (mT)	M_s ($Am^2\ kg^{-1}$)
1	573 K	623 K	623 K	–	–	7	0.2
2	673 K	–	–	523 K	673 K	10	0.4
3	623 K	–	–	–	623 K	0.7	32
4	673 K	–	–	623 K	623 K	0.4	3.3

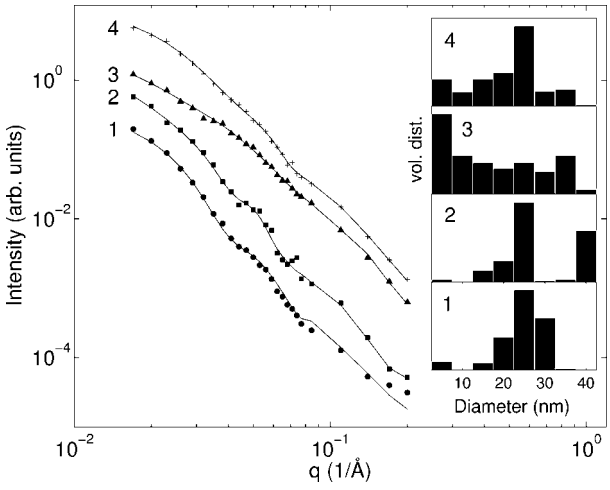

Figure 4
Ni–Ni PSF (symbols) solved from ASAXS intensities and the corresponding Monte Carlo fits (solid lines). Inset shows the number distribution $\nu(R)$ histogram multiplied by particle volume on linear scale.

fibrous cellulose might assist the separate growth of particles inside the fibers so that the particles are not as aggregated as on the surface of the fibers (Fig. 1). However, cellulose does not affect the crystallization temperature of the particles as the crystallization begins at similar temperatures as observed with self-supported Ni and Ni–P particles (Hur *et al.*, 1990).

The magnetization curves of the pristine samples are shown in Fig. 5. Samples 1 and 2 made in H_2O had a small ferromagnetic component, while a large ferromagnetic component was observed in samples 3 and 4. The magnetic parameters extracted from the curves are given in Table 2.

The coercivity H_c depends on the crystalline order of the ferromagnetic material. For amorphous material the coercivity is lower than for crystalline material. For bulk fcc nickel the saturation magnetization, M_s, is 55 $Am^2\ kg^{-1}$, while for amorphous bulk nickel M_s has been reported to be 60% of that (Tamura & Endo, 1969; Rojo *et al.*, 1996). This is in good agreement with the saturation magnetization M_s observed for sample 3, but not for sample 1, although both samples contained mostly fcc Ni after annealing according to WAXS results. Obviously the phosphorus in sample 3 does not have a significant effect on the magnetization, but in sample 1 during heating the oxide phase and the metastable hcp Ni phase appeared indicating a difference in the structure in the pristine samples 1 and 3. Hcp Ni nanoparticles of size about 9 nm have been shown to be paramagnetic (Jeon *et al.*, 2006). On the other hand, Roy *et al.* (2005) assigned an oxygen-stabilized tetragonal crystal structure for Ni particles obtained using the borohydride reduction to explain the paramagnetism of their 20 nm sized self-supported particles.

Table 3
ASAXS measurement energies with respective anomalous scattering factors f' and f'' determined for samples 1 and 3.

The values of f' and f'' determined for sample 3 were used also for samples 2 and 4.

E (eV)	f'_1	f''_1	f'_3	f''_3	f'_{theor}	f''_{theor}
7902.3	−2.61	0.52	−2.60	0.53	−2.6678	0.5262
8272.7	−4.54	0.48	−4.57	0.49	−4.6157	0.4844
8322.2	−6.172	0.51	−6.306	0.55	−6.4244	0.4792
8325.7	−6.511	0.55	−6.697	0.60	−6.8351	0.4788

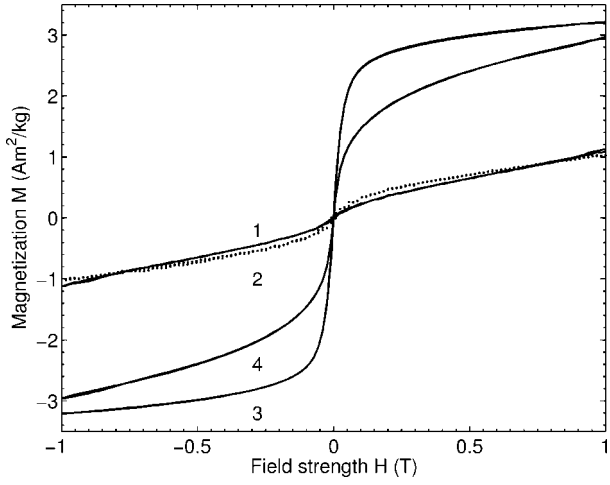

Figure 5
Magnetization measured for each sample. The curve for sample 2 is drawn with dots for clarity (every second point) and the curve of sample 3 was multiplied by 0.1 for better visualization.

Sample 2 contained almost purely nickel phosphides and only a small amount of fcc Ni appeared upon heating, which explains why only a small ferromagnetic contribution was observed. Sample 4 behaved both magnetically and crystallographically as a mixture of samples 2 and 3. By comparing with the X-ray diffraction data by Hur *et al.* (1990) we see that the phosphorus content in the Ni-containing nanoparticles is about 23 at% or more in sample 2, between 11 and 17.5 at% in sample 3, and between 17.5 and 19 at% in sample 4.

5. Conclusions

In this work fibrous cellulose was successfully used as a support for amorphous nickel nanoparticles. The reduction conditions affected the coordination of Ni atoms, the composition of the nanoparticles and the particle size distribution. The phosphorus content in the Ni nanoparticles reduced with hypophosphite was significantly lower in samples reduced in aqueous ammonium medium compared with the sample reduced in water. The samples made in aqueous ammonium medium were ferromagnetic. However, according to ASAXS and SEM results the Ni particle sizes ranged in these samples from a few nanometres to micrometre clusters, while in samples made in H_2O fewer particles with size smaller than 15 nm were observed. When borohydride was used as a reducing agent the particles were more monodisperse compared with reduction with hypophosphite.

We thank the HASYLAB organization for the possibility to perform the measurements and Dr G. Goerigk for help during and

after the measurements. The Academy of Finland (project 104837) is acknowledged for financial support.

References

Bazin, D. C., Sayers, D. A. & Rehr, J. J. (1997). *J. Phys. Chem. B*, **101**, 11040–11050.

Brennan, S. & Cowan, P. L. (1992). *Rev. Sci. Instrum.* **63**, 850–853.

Chantler, C. T., Olsen, K., Dragoset, R. A., Kishore, A. R., Kotochigova, S. A. & Zucker, D. S. (2005). X-ray form factor, attenuation and scattering tables (Version 2.1). National Institute of Standards and Technology, Gaithersburg, MD. Originally published as Chantler, C. T. (2000). *J. Phys. Chem. Ref. Data*, **29**, 597–1048; and Chantler, C. T. (1995). *J. Phys. Chem. Ref. Data*, **24**, 71–643.

Evans, G. & Pettifer, R. F. (2001). *J. Appl. Cryst.* **34**, 82–86.

Fuoss, P., Eisenberg, P., Warburton, W. K. & Bienenstock, A. (1981). *Phys. Rev. Lett.* **46**, 1537–1540.

Glavee, G. N., Klabunde, K. J., Sorensen, C. M. & Hadjipanayis, G. C. (1994). *Langmuir*, **10**, 4726–4730.

Goia, D. V. & Matijević, E. (1998). *New J. Chem.* **22**, 1203–1215.

Gong, W., Li, H., Zhao, Z. & Chen, J. (1991). *J. Appl. Phys.* **69**, 5119–5121.

Guinier, A. (1994). *X-ray Diffraction* in *Crystals, Imperfect Crystals, and Amorphous Bodies*. New York: Dover Publications Inc.

Haubold, H.-G., Gruenhagen, K., Wagener, M., Jungbluth, H., Heer, H., Pfeil, A., Rongen, H., Brandenberg, G., Moeller, R., Matzerath, J., Hiller, P. & Halling, H. (1989). *Rev. Sci. Instrum.* **60**, 1943–1946.

Hur, K.-H., Jeong, J.-H. & Lee, D. N. (1990). *J. Mater. Sci.* **25**, 2573–2584.

Illy, S., Tillement, O., Machizaud, F., Dubois, J., Massicot, F., Fort, Y. & Ghanbaja, J. (1999). *Philos. Mag. A*, **79**, 1021–1031.

Jeon, Y. T., Moon, J. Y., Lee, G. H., Park, J. & Chang, Y. (2006). *J. Phys. Chem. B*, **110**, 1187–1191.

Kraft, S., Stümpel, J., Becker, P. & Kuetgens, U. (1996). *Rev. Sci. Instrum.* **67**, 681–687.

Leslie-Pelecky, D. L. & Rieke, R. D. (1996). *Chem. Mater.* **8**, 1770–1783.

Mansour, A. & Melendres, C. (1998). *J. Phys. Chem. A*, **102**, 65–81.

Martelli, S. & di Nunzio, P. E. (2002). *Part. Part. Syst. Charact.* **19**, 247–255.

Modrow, H. (2004). *Appl. Spectrosc. Rev.* **39**, 183–290.

Munro, R. G. (1982). *Phys. Rev. B*, **25**, 5037–5045.

Neumaier, A. (1998). *SIAM Review*, **40**, 636–666.

Rojo, J., Hernando, A., El Ghannami, M., Carcía-Escorial, A. & González, M. (1996). *Phys. Rev. Lett.* **76**, 4833–4836.

Roy, A., Srinivas, V., Ram, S., De Toro, J. & Mizutani, U. (2005). *Phys. Rev. B*, **71**, 184443.

Sarkar, A., Kapoor, S., Yashwant, G., Salunke, H. & Mukherjee, T. (2005). *J. Phys. Chem. B*, **109**, 7203–7207.

Serimaa, R., Eteläniemi, V., Serimaa, O., Laitalainen, T. & Bienenstock, A. (1996). *J. Appl. Cryst.* **29**, 309–402.

Simon, J. P. & Lyon, O. (1994). In *Resonant Anomalous X-ray Scattering*. North-Holland: Elsevier Science VB.

Tamura, K. & Endo, H. (1969). *Phys. Lett. A*, **29**, 52–53.

Tatchev, D., Goerigk, G., Valova, E., Dille, J., Armyanov, R. K. S. & Delplancke, J.-L. (2005). *J. Appl. Cryst.* **38**, 787–794.

Xie, S., Qiao, M., Zhou, W., Luo, G., He, H., Fan, K., Zhao, T. & Yuan, W. (2005). *J. Phys. Chem. B*, **109**, 24361–24368.